

REPORT DOCUMENTATION PAGE			Form Approved OMB No. 0704-0188	
Public reporting burden for this collection of information is estimated to average 1 hour per response, including the time for reviewing instructions, searching existing data sources, gathering and maintaining the data needed, and completing and reviewing this collection of information. Send comments regarding this burden estimate or any other aspect of this collection of information, including suggestions for reducing this burden to Department of Defense, Washington Headquarters Services, Directorate for Information Operations and Reports (0704-0188), 1215 Jefferson Davis Highway, Suite 1204, Arlington, VA 22202-4302. Respondents should be aware that notwithstanding any other provision of law, no person shall be subject to any penalty for failing to comply with a collection of information if it does not display a currently valid OMB control number. <b>PLEASE DO NOT RETURN YOUR FORM TO THE ABOVE ADDRESS.</b>				
1. REPORT DATE (DD-MM-YYYY) 29-Sep-2006		2. REPORT TYPE REPRINT		3. DATES COVERED (From - To)
4. TITLE AND SUBTITLE DETERMINATION OF CRUST AND UPPER MANTLE STRUCTURE BENEATH AFRICA USING A GLOBAL OPTIMIZATION BASED WAVEFORM MODELING TECHNIQUE		5a. CONTRACT NUMBER FA8718-04-C-0014		
		5b. GRANT NUMBER		
		5c. PROGRAM ELEMENT NUMBER 62601F		
6. AUTHOR(S) Jay Pulliam, Mrinal K. Sen, and Abhijit Gangopadhyay		5d. PROJECT NUMBER 1010		
		5e. TASK NUMBER SM		
		5f. WORK UNIT NUMBER A1		
7. PERFORMING ORGANIZATION NAME(S) AND ADDRESS(ES)  University of Texas at Austin 4412 Spicewood Springs Rd., Building 600 Austin, TX 78759-8500		8. PERFORMING ORGANIZATION REPORT NUMBER		
9. SPONSORING / MONITORING AGENCY NAME(S) AND ADDRESS(ES) Air Force Research Laboratory 29 Randolph Road Hanscom AFB, MA 01731-3010		10. SPONSOR/MONITOR'S ACRONYM(S) AFRL/VSBYE		
		11. SPONSOR/MONITOR'S REPORT NUMBER(S) AFRL-VS-HA-TR-2006-1160		
12. DISTRIBUTION / AVAILABILITY STATEMENT Approved for Public Release; Distribution Unlimited.				
13. SUPPLEMENTARY NOTES Reprinted from: Proceedings of the 28 <sup>th</sup> Seismic Research Review – Ground-Based Nuclear Explosion Monitoring Technologies, 19 – 21 September 2006, Orlando, FL, Volume I pp 196 - 208.				
14. ABSTRACT During the initial years of the project, a waveform modeling program based on the reflectivity method and incorporating a global optimization algorithm, was developed. Assuming a one-dimensional, isotropic, layered Earth, the method computes synthetic seismograms by distributing independent computations for different ray parameters across multiple processors, providing nearly a linear decrease in computation time with the number of processors. During the inversion process, the method implements a global optimization algorithm using very fast simulated annealing (VFSA). Global optimization allows for searching within a broad spectrum of models in order to find the global minimum, and eliminates dependency on the starting model. In particular, VFSA is advantageous because it allows for larger sampling of the model space during the early stages of the inversion process, and much narrower sampling in the model space as the inversion converges and the temperature decreases, while still allowing the search to escape local minima. Additionally, the ability of VFSA to perform different perturbations for different model parameters allows for individual control of each parameter and the incorporation of <i>a priori</i> information. The method also uses statistical tools such as computation of the posterior probability density (PPD) function and the parameter correlation matrix, so as to evaluate the uniqueness of a particular model obtained by searching the model space, and the trade-offs between individual model parameters therein. The waveform modeling approach has now been applied to ground truth data recorded in twelve permanent broadband seismographic stations spanning the African continent. The waveforms modeled included S, Sp, SsPmP, and shear-coupled PL (SPL) phases from deep (200–800 km) earthquakes of magnitude 5.5 to 7.0 located at distances of 30 to 80 degrees. Earthquake data that satisfy the search criteria described above are sparse, however. Seventeen events meeting the above criteria were available for analysis. Forward computation of the synthetic seismograms was performed using models from independent receiver function studies (wherever available) as an initial velocity model for the crust. Preliminary reference earth model (PREM) was used for mantle velocities below the receiver function models. The global optimization algorithm with several hundreds of iterations was then implemented. This algorithm perturbs the crust and upper mantle velocity structure (up to ~100 km depth) within user-specified bounds to generate synthetic seismograms that best fit the data. The results show that the final velocity models obtained from the application of this method for various stations in the African continent correlate well with those obtained from receiver function techniques. In particular, more detailed crust and upper mantle structure was obtained for seismographic stations located in north and west Africa, where prior studies are sparse. Broad tectonic observations were supported by the models generated using this method; specific refinements of the models for some stations are underway. Overall, the method is successful in determining the crust and upper mantle structure of the African continent. Notable advantages of this method include ability to simultaneously model all the waveforms, assess uncertainties in model parameters, finding a range of acceptable models that explain the data, and avoiding a dependence of the final model on the starting model. Furthermore, it differs from other commonly used methods in the fact that it provides a direct measurement of P and S wave velocities simultaneously. Also, the use of the SPL phase wherever available improves constraints on the models of the lower crust and upper mantle.				
15. SUBJECT TERMS Seismic velocity, Seismic propagation				
16. SECURITY CLASSIFICATION OF:			17. LIMITATION OF ABSTRACT  SAR	18. NUMBER OF PAGES  13
a. REPORT UNCLAS	b. ABSTRACT UNCLAS	c. THIS PAGE UNCLAS		
			19a. NAME OF RESPONSIBLE PERSON Robert J. Raistrick	
			19b. TELEPHONE NUMBER (include area code) 781-377-3726	



**DETERMINATION OF CRUST AND UPPER MANTLE STRUCTURE BENEATH AFRICA USING A  
GLOBAL OPTIMIZATION BASED WAVEFORM MODELING TECHNIQUE**

Jay Pulliam, Mrinal K. Sen, and Abhijit Gangopadhyay

University of Texas at Austin

Sponsored by Air Force Research Laboratory

Contract No. FA8718-04-C-0014

**ABSTRACT**

During the initial years of the project, a waveform modeling program based on the reflectivity method and incorporating a global optimization algorithm, was developed. Assuming a one-dimensional, isotropic, layered Earth, the method computes synthetic seismograms by distributing independent computations for different ray parameters across multiple processors, providing nearly a linear decrease in computation time with the number of processors. During the inversion process, the method implements a global optimization algorithm using very fast simulated annealing (VFSA). Global optimization allows for searching within a broad spectrum of models in order to find the global minimum, and eliminates dependency on the starting model. In particular, VFSA is advantageous because it allows for larger sampling of the model space during the early stages of the inversion process, and much narrower sampling in the model space as the inversion converges and the temperature decreases, while still allowing the search to escape local minima. Additionally, the ability of VFSA to perform different perturbations for different model parameters allows for individual control of each parameter and the incorporation of *a priori* information. The method also uses statistical tools such as computation of the posterior probability density (PPD) function and the parameter correlation matrix, so as to evaluate the uniqueness of a particular model obtained by searching the model space, and the trade-offs between individual model parameters therein.

The waveform modeling approach has now been applied to ground truth data recorded in twelve permanent broadband seismographic stations spanning the African continent. The waveforms modeled included S, Sp, SsPmP, and shear-coupled PL (SPL) phases from deep (200–800 km) earthquakes of magnitude 5.5 to 7.0 located at distances of 30 to 80 degrees. Earthquake data that satisfy the search criteria described above are sparse, however. Seventeen events meeting the above criteria were available for analysis. Forward computation of the synthetic seismograms was performed using models from independent receiver function studies (wherever available) as an initial velocity model for the crust. Preliminary reference earth model (PREM) was used for mantle velocities below the receiver function models. The global optimization algorithm with several hundreds of iterations was then implemented. This algorithm perturbs the crust and upper mantle velocity structure (up to ~100 km depth) within user-specified bounds to generate synthetic seismograms that best fit the data. The results show that the final velocity models obtained from the application of this method for various stations in the African continent correlate well with those obtained from receiver function techniques. In particular, more detailed crust and upper mantle structure was obtained for seismographic stations located in north and west Africa, where prior studies are sparse. Broad tectonic observations were supported by the models generated using this method; specific refinements of the models for some stations are underway.

Overall, the method is successful in determining the crust and upper mantle structure of the African continent. Notable advantages of this method include ability to simultaneously model all the waveforms, assess uncertainties in model parameters, finding a range of acceptable models that explain the data, and avoiding a dependence of the final model on the starting model. Furthermore, it differs from other commonly used methods in the fact that it provides a direct measurement of P and S wave velocities simultaneously. Also, the use of the SPL phase wherever available improves constraints on the models of the lower crust and upper mantle.



## **OBJECTIVES**

We describe a technique based on waveform fitting by synthetic seismograms, and demonstrate its application to determine the crust and upper mantle structure beneath the continent of Africa. Our technique utilizes the reflectivity method (Kennett, 1983) to compute the synthetic seismograms for an earthquake recorded at a particular seismic station and implements a global optimization algorithm using VFSA (Ingber, 1989; Sen and Stoffa, 1995) to invert for the crust and upper mantle structure beneath the station. Our technique is complimentary to the existing receiver function analysis method (e.g., Owens et al., 1987; Ammon, 1991) and retains its advantages, yet minimizes its potential limitations when the derived structural models are used to locate and determine the focal depths of small, regional events.

## **RESEARCH ACCOMPLISHED**

### **Modeling Method**

Following the development of the forward problem described in Pulliam and Sen (2005), we perform an optimization procedure to determine the best model for a given source-receiver pair. In this analysis we employ a “global optimization algorithm” which is only weakly dependent on the choice of the initial model. In particular, we use a method called VFSA, which is a variant of simulated annealing (SA) aimed at making the computations more efficient (Ingber, 1989; Sen and Stoffa, 1995). To further illustrate the VFSA technique, a simplified flow-chart is shown in Figure 1. The method starts with an initial model ( $m^0$ ) with an associated error or energy,  $E(m^0)$ . It then draws a new model,  $m^{\text{new}}$ , among a distribution of models from a temperature ( $T$ ) dependent Cauchy-like distribution,  $r(T)$ , centered on the current model (Figure 1). The associated error or energy,  $E(m^{\text{new}})$ , is then computed and compared with  $E(m^0)$  (Figure 1). If the change in energy ( $\delta E$ ) is less than or equal to zero, the new model is accepted and replaces the initial model. However, if the above condition is not satisfied,  $m^{\text{new}}$  is accepted with a probability of  $[e^{\delta E/T}]$  (Figure 1). This rule of probabilistic acceptance in SA allows it to escape a local minimum. The processes of model generation and acceptance are repeated a large number of times with the annealing temperature gradually decreasing according to a predefined cooling schedule (Figure 1). VFSA is more efficient than the traditional SA because it allows for larger sampling of the model space during the early stages of the waveform fitting, and much narrower sampling in the model space as the procedure converges and the temperature decreases, while still allowing the search to escape from the local minima. Additionally, the ability to perform different perturbations for different model parameters allows for individual control of each parameter and the incorporation of *a priori* information (Sen and Stoffa, 1995).

Solutions to geophysical inverse problems are often nonunique. It is therefore necessary to explore the model space and thus identify the range of models that fit the data, and perhaps to identify characteristics of the models that are required by the data, rather than which simply are allowed by the data. VFSA conducts such a search efficiently, and the products of multiple such searches enable us to evaluate the uncertainty in a single, best-fitting solution. This evaluation is particularly necessary in seismic waveform modeling because more than one model can often explain the observed data equally well, and trade-offs between different model parameters are common (Pulliam and Sen, 2005). The waveform inversion method we use in this study incorporates important statistical tools that allow the user to evaluate the uniqueness, and physical feasibility of the resulting model. The most useful of these tools in evaluating the results’ reliability are the posterior probability density (PPD) function, and the parameter correlation matrix. To estimate these statistical parameters we cast the inverse problem in a Bayesian framework (e.g., Sen and Stoffa, 1995), and employ “importance sampling” based on a Gibbs’ sampler (GS) (Sen and Stoffa, 1995; Pulliam and Sen, 2005). The goal of “importance sampling” is to concentrate sample points in the regions that are the most “significant,” in some sense (perhaps, for example, where the error function is rapidly varying, or many acceptable solutions lie). Because this concentration is achieved using a Gibbs’ probability distribution, it has been named the “Gibbs’ sampler” (Sen and Stoffa, 1995). The PPD function  $[\sigma(\mathbf{m}|\mathbf{d}_{\text{obs}})]$  is defined as a product of a likelihood function  $[e^{-E(\mathbf{m})}]$ , and prior probability density function,  $p(\mathbf{m})$ . The prior probability density function  $p(\mathbf{m})$ , describes the available information on the model without the knowledge of the data and defines the probability of the model  $\mathbf{m}$  independent of the data. The likelihood function defines the data misfit and its choice depends on the distribution of error in the data (Sen and Stoffa, 1995). Sen and Stoffa (1996) examined several different approaches to sampling models from the PPD and concluded that a multiple-VFSA based approach, though theoretically approximate, is the most efficient. Here, we have employed the fast multiple-VFSA algorithm to estimate uncertainties. We compute approximate marginal PPD and posterior correlation matrices to characterize uncertainties in the derived results. The



posterior correlation matrix measures the relative trade-off between individual model parameters and is computed by normalizing the covariance between two model parameters (Sen and Stoffa, 1996).

### Application

We apply the modeling method outlined above to data from large-magnitude, deep-focus earthquakes recorded teleseismically at twelve permanent broadband seismic stations spanning the continent of Africa (Figure 2). A total of seventeen earthquakes are used in this study selected from the global catalog of Harvard Centroid Moment Tensors (CMT) (1976–2004) (Table 1). Seven of these are located in the Hindu Kush, three in southern Bolivia, two each in Argentina, and the Java Sea, and one each in Afghanistan, South Sandwich Islands, and southern Sumatra. The focal depths of these earthquakes range between 200 km–600 km, and their magnitudes lie between 5.5–7.0. Since the goal of this study is to also model the SPL phase that is generated close to the seismic station, we choose such a focal depth range to eliminate the (SPL) phase generated at the earthquake source. Epicentral distances from the seismic stations of the selected earthquakes are between 30° and 80° so as to avoid possible incorporation of phases that interacted with the earth's core. Based on our selection criteria, earthquake data available from the seismic stations in Africa are sparse. Hence, the numbers of earthquakes recorded by each station range from 1 to 9 and azimuthal coverage is poor. In spite of the sparse set of source-receiver pairs available for modeling, we are able to obtain reliable azimuthally dependent models in some cases.

**Table 1. List of earthquakes used in this study**

Event Number	Date (yyyy/mm/dd)	Time (hr:min:sec)	Latitude	Longitude	Focal Depth (km)	Magnitude	Region
1	1990/07/13	14:27:24.8	36.46 N	70.80 E	218	5.6	Hindu Kush
2	1991/06/23	21:31:58.33	26.82 S	63.40 W	581	6.4	Santiago del Estero, Argentina
3	1993/08/09	11:44:08.306	36.42 N	70.72 E	210	5.8	Hindu Kush
4	1993/08/09	12:48:29.404	36.36 N	70.85 E	230	6.3	Hindu Kush
5	1994/06/30	09:31:04.212	36.25 N	71.08 E	233	6.1	Afghanistan
6	1994/10/25	00:58:47.987	36.30 N	70.91 E	244	5.9	Hindu Kush
7	1994/11/15	20:27:46.338	5.61 S	110.2 E	559	6.2	Java Sea
8	1994/12/07	03:47:10.307	23.46 S	66.74 W	243	5.6	Jujuy Province, Argentina
9	1995/05/13	21:07:41.552	5.22 S	108.92 E	554	5.7	Java Sea
10	1997/01/23	02:24:53.890	22 S	65.72 W	276	6.4	Southern Bolivia
11	1997/10/05	18:14:56.228	59.74 S	29.20 W	273.9	6.0	South Sandwich Islands
12	1997/12/17	05:55:49.933	36.39 N	70.77 E	207	5.5	Hindu Kush
13	1998/03/21	18:26:09.8	36.43 N	70.13 E	227.8	5.8	Hindu Kush
14	1999/09/15	03:11:17.074	20.93 S	67.28 W	218	6.0	Southern Bolivia
15	2002/03/03	12:12:00.183	36.43 N	70.44 E	209	6.3	Hindu Kush
16	2003/07/27	11:49:52.347	20.13 S	65.18 W	345.3	5.9	Southern Bolivia
17	2004/07/25	14:44:40.148	2.43 S	103.98 E	582.1	6.8	Southern Sumatra, Indonesia

### Results of this Application

Below, we report results of waveform fitting for selected teleseismic earthquakes recorded in Africa. A comment on amplitude matches: The most successful match between synthetics and data would be one in which the synthetic waveform matched the data exactly—wiggles for wiggles. This is unrealistic for several reasons, including the fact that models used to compute synthetics are layered, isotropic, limited to ten to sixteen layers, and have fixed attenuation ( $Q$ ) values. Further, the source time function is assumed to be Gaussian and its focal mechanism is assumed to be correctly represented by Harvard's CMT solution. To minimize complexities in the source time function we avoid very large earthquakes. Given the uncertainties in model  $Q$  and focal mechanisms, which will largely control relative amplitudes of various phases, we focus our fitting criteria on matching each phase's arrival time, polarity, and pulse character. Fitting the amplitude of each phase, while desirable, is deemed to be of lesser importance.



### West Africa

The region encompassing north and west Africa includes the seismic stations of TAM, DBIC, MBO, and MDT (Figure 2). Among these stations, TAM recorded data of better quality; examples of the waveform fits for events 1, 3, and 6 (Table 1) recorded at TAM are shown in Figure 3a. We observe S, SP, and SsPmP phases consistently on all these event seismograms, and they correlate well with the synthetics generated by the optimization technique (Figure 3a). On event 3, we also observe a prominent SPL phase and the synthetics match it well (Figure 3a). Particle motion diagrams for the corresponding time window on both data and synthetics confirm this observation (Figure 3b). We observe prograde elliptical particle motion, which is diagnostic of the SPL phase, on both diagrams (Figure 3b). Except for event 3, none of the others have any signature of the SPL phase, as confirmed by particle motion diagrams for corresponding time windows. This observation—that one source-receiver pair would show SPL while other, similar paths would not—is unexpected and we cannot explain it.

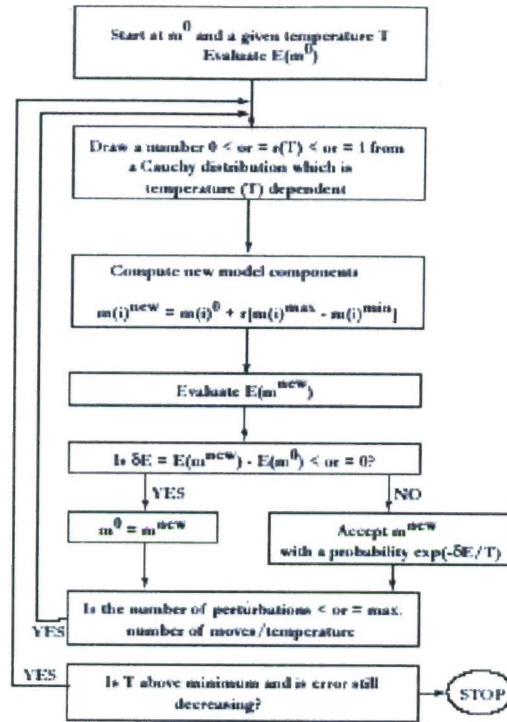
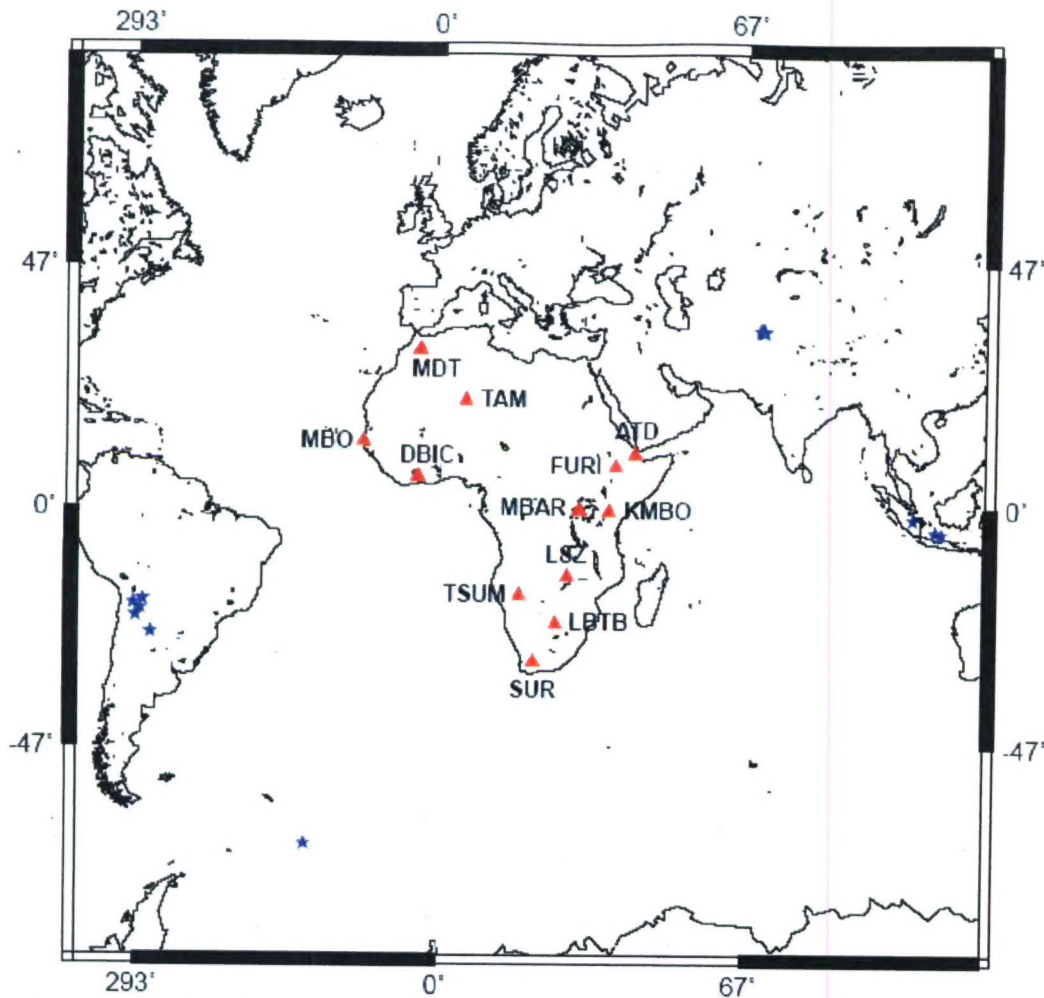


Figure 1. Flow-chart elaborating the very fast simulated annealing (VFSA) algorithm used in this study for the waveform inversion by global optimization (Modified from Sen and Stoffa, 1995).  $E(m^0)$ -error function for the initial model  $m^0$ ,  $E(m^{\text{new}})$ -error function for the new model  $m^{\text{new}}$ ,  $T$ -temperature,  $r(T)$ -temperature dependent Cauchy-like distribution.





**Figure 2.** Map showing locations of the earthquakes used in this study (blue stars) and the permanent broadband seismic stations in the African continent (red triangles) that have recorded these earthquakes. The respective station codes are shown adjacent to each seismic station.

Based on the waveform-fitting results for all six events recorded at TAM, we generate P- and S-wave velocity models up to a depth of 100 km (Figure 3c). We observe some variability in the models (Figure 3c), and hence compute the uncertainties for each model using the statistical tools described earlier to choose the “best” model. In Figure 3d, we show examples of parameter correlation matrices computed from the modeling results of events 1 and 3 (Table 1). Each small square along an axis of the parameter correlation matrix, either horizontally or vertically, represents a model parameter (Figure 3d). Since every model layer consists of four independent model parameters ( $V_p$ ,  $V_s$ , thickness, and density), four small squares combined together represent a model layer on both axes (Figure 3d). Correlation values range between  $-1$  and  $1$  and are symmetric about the diagonal of the matrix, hence, for clarity, we show only values below the diagonal (Figure 3d). Values along the diagonal are ones, simply indicating that each parameter is perfectly correlated with itself. Off-diagonal colored squares indicate significant cross-correlation (trade-offs) between corresponding model parameters. In the parameter correlation matrices for both events (Figure 3d), layers comprising the upper crust have greater independence, as indicated by the sparse distribution of off-diagonal cross-correlations whose absolute values are greater than  $\pm 0.5$  (colored squares). Also, for both events, the level of tradeoffs among model parameters in these shallow layers is similar (Figure 3d). For event 1, however, the layers comprising the lower crust and upper mantle have larger off-diagonal cross-correlations, indicating significant tradeoffs (Figure 3d). On the contrary, for event 3, even the lower crustal and upper mantle layers appear better constrained (Figure 3d). Intriguingly, the SPL phase is also observed in the



seismogram of event 3 but not in that of event 1 (Figure 3a). This observation attests to the fact that, if SPL is present in the seismogram and is well modeled, we are able to better constrain the structure of the lower crust and upper mantle. This result, which is expected, due to the sensitivity of SPL to those parts of the model (Figure 1b), drives our decision to generate velocity models down to the Moho for seismic stations at which SPL is not observed.

We observe and successfully fit S and SP phases in seismograms recorded at DBIC and at MBO. The SsPmP phase appears on the vertical-component seismograms of events 13 at DBIC and event 16 at MBO but is absent on their radial-component seismograms. We do not observe the SPL phase in seismograms recorded at DBIC but do so at MBO in the seismograms of event 16. The SPL phase is prominent on both vertical and radial component seismograms of event 16 recorded at MBO, which we confirm with particle motion diagrams that show prograde elliptical motion for the corresponding time window. At MDT, within the time-window expected to contain the phases analyzed in this study, we are unable to clearly identify them and they appear to be contaminated by interfering arrivals, and hence are also not well-correlated with the synthetics generated by the waveform inversion process. Station MDT is located near the Atlas Mountains in Morocco, and so may be underlain by complicated three-dimensional structure, which the waveform modeling program used in this study is unable to model accurately. The lack of correlation between synthetic seismograms and data at MDT is likely a consequence of this limitation.

### East Africa

Stations ATD, FURI, KMBO, and MBAR are situated within and on the flanks of the active East African rift system and waves recorded at these stations sample the complicated three-dimensional, anisotropic structure beneath the rift (Ayele et al., 2004; Dugda and Nyblade, 2006). Three-dimensional structure is manifested in the seismograms as numerous, possibly scattered, refracted, or split, phase arrivals with strong interference amongst themselves. Anisotropy inferred from shear-wave splitting studies has also been reported for stations ATD, FURI, and KMBO by Ayele et al. (2004). The waveform inversion method we use in this study is capable of estimating only one-dimensional (although azimuthally dependent) structure only, hence waveforms for events recorded at these stations are not precisely correlated in some cases. On both the vertical and radial component seismograms of most events at ATD, FURI, KMBO, and MBAR, we observe S and SsPmP phases. On the other hand, except at MBAR, we observe the SP phase only on the vertical component for these events. Only at FURI, for event 12 (Table 1), and MBAR, for event 15 (Table 1), do we see SPL phases in the seismograms.

### Southern Africa

Seismic stations TSUM, LSZ, LBTB, and SUR are located in southern Africa (Figure 2). However, for the lone event recorded at SUR, we are able to identify only the direct S phase, and thus we do not attempt to generate P- and S-wave velocity models for SUR. We observe and successfully fit S, SP, and SsPmP phases on events 13 and 14 (Table 1) recorded at TSUM, event 9 (Table 1) recorded at LSZ, and event 11 (Table 1) at LBTB. But, except for event 13 at TSUM, we are able to identify the SP phase on both the vertical and radial component seismograms at TSUM, LSZ, and LBTB. Similarly, the SsPmP phase is only identifiable on the vertical component seismogram for events 14 and 9 recorded at TSUM and LSZ respectively. It is, however, absent on the seismograms for event 13 at TSUM. We do not observe the SPL phase in the seismograms of any event recorded at these stations.

### Summary of Models

Figures 4a–d show P- and S-wave velocity models for the north and west African stations of TAM, DBIC, MBO, and MDT. Estimates of crustal thickness beneath these stations range between 36 km and 42 km (Figures 4a–d), comparable to regional estimates of 34 km to 40 km by Pasyanos et al. (2004). We also note that the crust is slightly thicker in west Africa, e.g. beneath stations DBIC and MBO (~41–42 km) (Figures 4b and 4c), compared to the seismic stations TAM and MDT in north Africa (~36 km–38 km) (Figures 4a and 4d). A similar observation was also made earlier by Pasyanos and Walter (2002) using surface wave dispersion tomography, and by Marone et al. (2003) using joint inversion of local, regional, and teleseismic data. Except for TAM, the crust below all the stations appears to be fairly simple in structure (Figures 4a–d) (Sandvol et al., 1998), suggesting that it is minimally affected by large-scale tectonic processes. However, a middle to lower crustal low-velocity zone obtained beneath all the seismic stations in the region (Figures 4a–d), indicate possible local tectonic influences. Our estimate of crustal thickness beneath TAM (~36 km) is similar to that obtained from receiver function studies by Sandvol et al. (1998) ( $38 \pm 2$  km) (Figure 4a), from Rayleigh wave group velocity dispersion studies by Hazler et al. (2001) ( $43 \pm 5$  km), and from surface-wave dispersion tomography by Pasyanos and Walter (2002) (~40 km). TAM is close to the location of the Hoggar hot spot but, as noted by Sandvol et al. (1998), the crustal thickness indicates that a mantle plume has not significantly altered the crust here. However, in contrast to the model of Sandvol et al. (1998), the



crustal P- and S-wave velocities we obtain in this study at TAM are both slightly lower (Figure 4a). These velocities at TAM range between 6.25 km/s–6.8 km/s, and 3.1 km/s–3.9 km/s, respectively (Figure 4a). Upper mantle P-wave velocities exhibit a gradational increase with depth below the Moho, whereas the S-wave velocities are nearly constant (4 km/s–4.2 km/s) within that range of depths (Figure 4a). Furthermore, we also obtain an anomalous low-velocity zone of ~5 km thickness at the base of the upper crust (Figure 4a) that appears to be well constrained based on the uncertainty estimates described earlier (Figure 3d). However, we are unable to confirm the existence of this layer from any other independent studies.

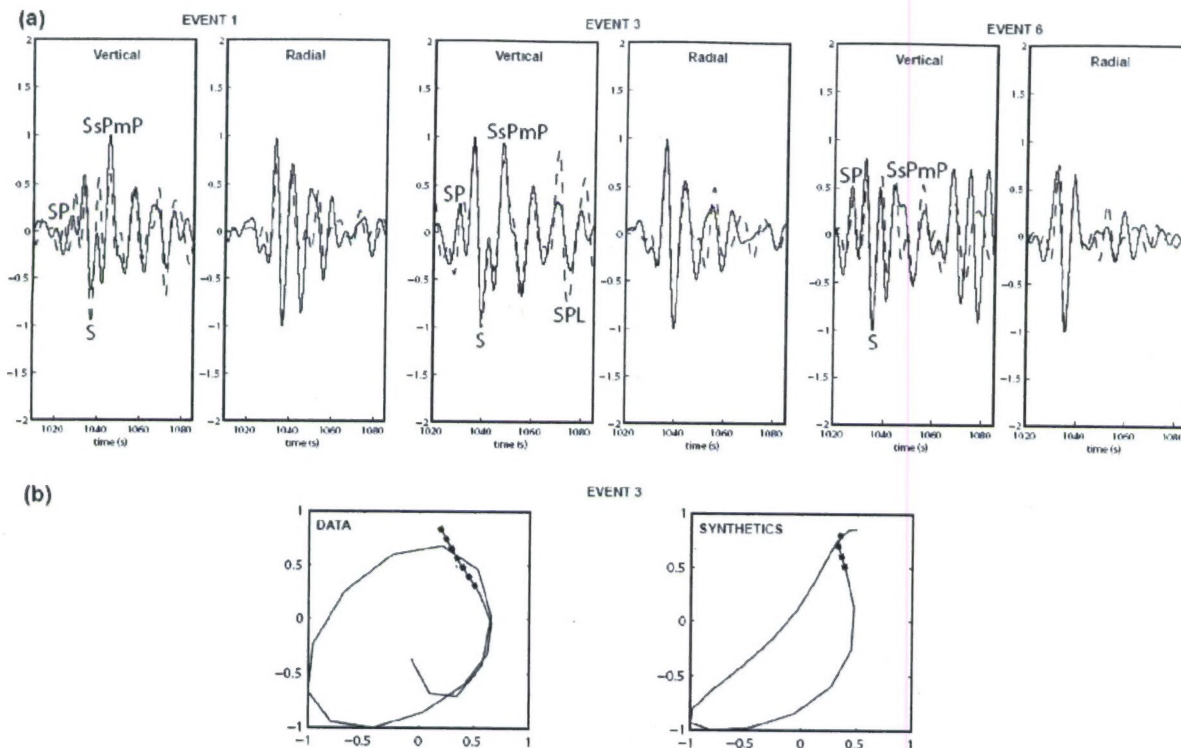


**Figure 3.** (a) Vertical and radial component seismograms for events 1, 3, and 6 (Table 1) recorded at TAM showing the observed (solid line) and synthetic (dashed line) waveforms. The correlated waveforms are indicated on the panels. (b) Particle motion diagrams for the portion of the waveforms in the time window (1077–1085 s) on the data and synthetics for event 3 showing prograde elliptical motion diagnostic of the SPL phase. The dotted portions of the diagrams indicate beginning of the motion. Figure 3 is continued on next page.



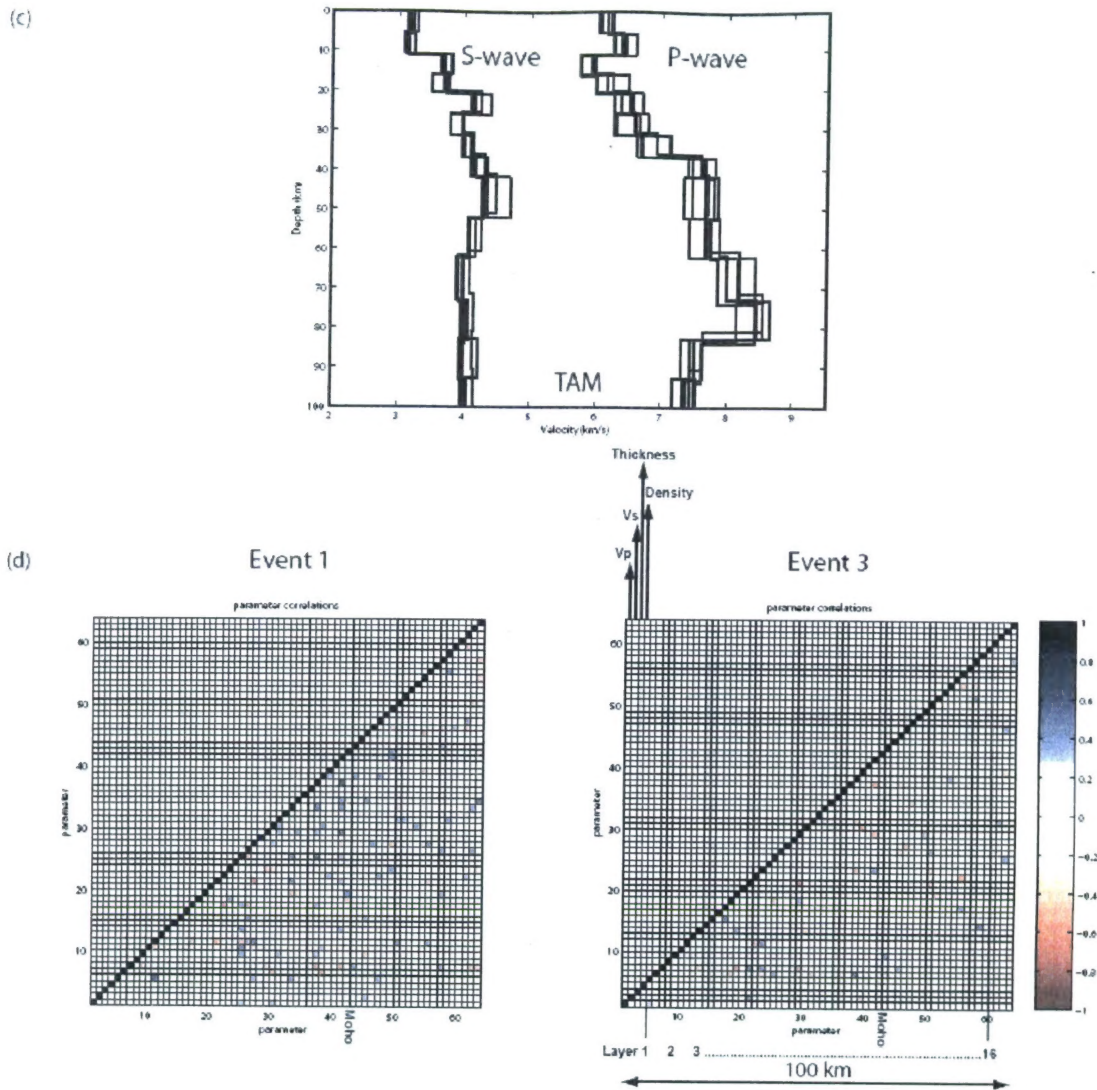


Figure 3 continued. (c) P- and S-wave velocity models up to 100 km for station TAM from the inversion results for individual events recorded at TAM. (d) Model parameter correlation matrices for events 1 (left panel) and 3 (right panel). Each small square represents a model parameter ( $V_p$ ,  $V_s$ , thickness of layer, and density) on both the axes. The correlations range between  $-1$  and  $1$ . Sparse off-diagonal colored squares in the lower crust-upper mantle in event 3 (right panel) compared to that in event 1 (left panel) indicate better resolution and confidence (less tradeoff) in this region.



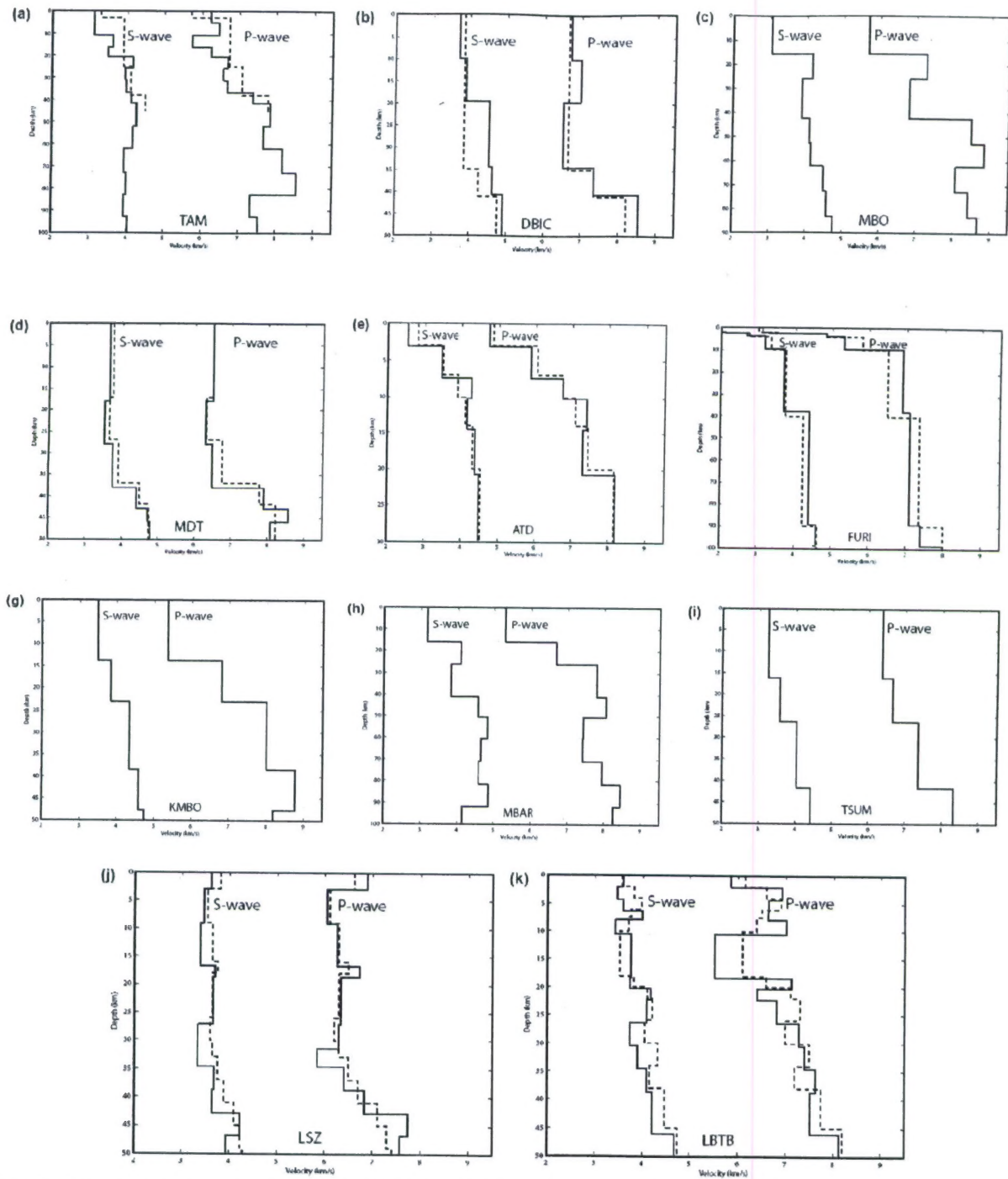


Figure 4. P- and S-wave velocity models (solid lines) obtained for (a) TAM (b) DBIC (c) MBO (d) MDT (e) ATD (f) FURI (g) KMBO (h) MBAR (i) TSUM (j) LSZ (k) LBTB. The P- and S-wave velocity models (broken lines) in (a), (b), (d), and (e) are from receiver function studies by Sandvol et al. (1998), in (f) are from receiver function studies by Ayele et al. (2004), and in (j) and (k) are from receiver function studies by Midzi and Ottemoller (2001).



At the west African coastal station DBIC, we obtain a Moho depth of  $\sim 41$  km which is similar to that obtained by Sandvol et al. (1998) ( $\sim 40 \pm 2.3$  km) (Figure 4b). P-wave velocities range between 6.7 km/s–7 km/s in the upper crust, and 6.5 km/s–7.3 km/s in the lower crust (Figure 4b). On the contrary, S-wave velocities show a gradational increase in the crust with depth from 3.7 km/s–4.7 km/s (Figure 4b). Anomalous  $V_p/V_s$  ratios are thus caused by a low P-wave velocity zone of  $\sim 15$  km thickness in the lower crust. However, due to the trade-offs between the model parameters in this depth range, we conclude that this anomaly is not well-constrained. Beneath MBO, any prior P- and/or S-wave velocity models are absent. Sandvol et al. (1998) had analyzed seismic data recorded at MBO but the anomalous data did not allow them to estimate a velocity model. We obtain a crustal thickness of  $\sim 42$  km (Figure 4c), which is similar to that found underneath other stations in the region. A regional crustal thickness of  $43 \pm 5$  km obtained from Rayleigh wave group velocity dispersion studies (Hazler et al., 2001) correlates well with the results of this study at MBO. The P- and S-wave velocities at MBO in the crust range between 5.6 km/s–7.2 km/s, and 3.1 km/s–4.1 km/s, respectively (Figure 4c). We also observe an anomalous lower crustal, approximately 15 km-thick zone of relatively low P- and S-wave velocities (6.8 km/s and 3.8 km/s) beneath MBO (Figure 4c). Our P- and S-wave velocity models beneath MDT predict a Moho depth of  $\sim 38$  km (Figure 4d). Surprisingly, even with the poor waveform fit by synthetics to the event recorded at MDT, this result is consistent with the estimates obtained by Sandvol et al. (1998) ( $36 \pm 1.3$  km). As also noted by Sandvol et al. (1998) and Pasyanos and Walter (2002), the slightly shallower Moho at MDT, compared to that at DBIC and MBO, indicates that in spite of its proximity to the Atlas Mountains, there is no crustal thickening associated with them, and a significant root is absent beneath the mountains. Sandvol et al. (1998) concluded that this may be a possible outcome of the fact that there existed a failed rift earlier which was subsequently inverted. In this study, beneath MDT, we obtain average P- and S-wave velocities in the crust of  $\sim 6.4$  km/s and 3.7 km/s, respectively, except in a low-velocity zone of  $\sim 10$  km thickness in the lower crust where these are 6.2 km/s and 3.4 km/s, respectively (Figure 4d). A similar zone has also been postulated by the earlier velocity model obtained from receiver function studies (Sandvol et al., 1998). However, because of poor waveform fits at MDT in this study, we are unable to postulate the existence of this zone.

For East Africa, we generate P- and S-wave velocity models beneath seismic stations ATD, FURI, KMBO, and MBAR, which are shown in Figures 4e–h. Located within and on the flanks of the East African Rift System, which is relatively well studied, these stations are situated in active tectonic domains. Except beneath ATD (Figure 4e), where the crust is significantly thin compared to the other stations in the region (Figures 4f–h), the Moho is generally between  $\sim 38$  km–41 km deep. The estimate of crustal thickness beneath ATD, however, is the subject of an active debate. Using a grid search method to model receiver functions for eleven earthquakes recorded at ATD, Sandvol et al. (1998) obtained a crustal thickness of  $\sim 10$  km (Figure 4e). But, Dugda and Nyblade (2006) used H- $\kappa$  analysis of receiver functions and predicted a crustal thickness of  $\sim 23 \pm 1.5$  km beneath ATD, consistent with earlier results from inversion of gravity data for the general area by Tiberi et al. (2005). In this study, our velocity model beneath ATD shows comparable velocity discontinuities at  $\sim 10$  km and  $\sim 21$  km depths (Figure 4e), suggesting that either of these depths could be interpreted as the Moho. However, the layer at 10 km depth appears to be poorly constrained compared to the layer at  $\sim 21$  km depth, as evidenced from the PPD and the parameter correlation matrix computations. Therefore, we prefer a crustal thickness of  $\sim 21$  km. Irrespective of the debate on the crustal thickness at ATD, the crust beneath it is significantly thinner than the crust beneath other seismic stations in east Africa (Figures 4f–h). Located within the Afar depression, close to the coast of the Red Sea on the eastern edge of the African continent, such a thin crust is expected at ATD because of highly stretched continental crust (Sandvol et al., 1998). The P- and S-wave velocities in the crust at ATD range between 4.7 km/s–7.2 km/s, and 2.5 km/s–4.3 km/s, respectively (Figure 4e). Crustal P-wave velocities below about 5 km depth are relatively high and, as noted by Dugda and Nyblade (2006), could indicate a highly mafic composition caused by igneous rock emplacement during the syn-rift stage. Figure 4f shows the preferred P- and S-wave velocity models beneath FURI which is situated in the northern part of the western Ethiopian plateau. We obtain an estimate of crustal thickness beneath FURI of  $\sim 39$  km, which is similar to that obtained using receiver function analyses by Ayele et al. (2004) ( $\sim 40$  km), and Dugda et al. (2005) ( $\sim 44$  km). The  $\sim 40$  km thick crust beneath FURI, which is located close to the border of the western Ethiopian plateau and the Afar depression, is also consistent with previous refraction studies of Berckhemer et al. (1975) as reported by Ayele et al. (2004). Crustal P- and S-wave velocities below  $\sim 5$  km depth at FURI range between 5.3 km/s–6.8 km/s, and 3.2 km/s–3.6 km/s, respectively (Figure 4f). In addition, beneath FURI, our results also predict an  $\sim 50$  km thick layer immediately below the Moho in the upper mantle that has P- and S-wave velocities of  $\sim 7.1$  km/s and  $\sim 4.3$  km/s, respectively, which are anomalously slow (Figure 4f). A similar layer with P- and S-wave velocities of  $\sim 7.4$  km/s and  $\sim 4.2$  km/s, respectively, was also obtained by Ayele et al. (2004) (Figure 4f). As noted by Ayele et al. (2004), this anomalously slow layer possibly indicates altered lithospheric material, and supports the result from Rayleigh wave dispersion by Knox et al. (1999), of an approximately 100 km thick



lithosphere beneath FURI. Station KMBO is located in Kenya, close to the southern end of the eastern branch of the East African Rift System, but outside its edge. Beneath KMBO our estimate of the crustal thickness is  $\sim 38$  km (Figure 4g). This estimate is similar to that obtained using receiver function analysis by Dugda et al. (2005) ( $\sim 41$  km). Crustal P- and S-wave velocities show a gradational increase with depth and range between 5.4 km/s–8 km/s, and 3.5 km/s–4.5 km/s, respectively (Figure 4g). The velocity structure beneath KMBO appears to be fairly simple. Although it has relatively high P-wave velocities in the lower crust (Figure 4g), it is otherwise typical of cratonic regions. Seismic station MBAR is located between the western boundary of the Tanzania craton and the western branch of the East African Rift System. Due to poor correlation of some of the observed phases with synthetics, and the availability of only one event, the velocity model beneath MBAR is poorly constrained. Nevertheless, our estimate of crustal thickness beneath MBAR, to our knowledge the first of its kind, is  $\sim 41$  km (Figure 4h), and is consistent with that obtained from other stations in the region. Crustal P- and S-wave velocities at MBAR range between 5.3 km/s–7.7 km/s, and 3.2 km/s–3.8 km/s, respectively (Figure 4h). Our model also predicts a low P-wave velocity ( $\sim 7.2$  km/s) layer beneath the crust (Figure 4h). Such a layer promotes the generation of the SPL phase near the station, which we observe in both data and synthetics for the event recorded at MBAR. Therefore, in spite of the poorly constrained model obtained in this study, we cannot rule out the possibility of its existence.

In southern Africa we generated P- and S-wave velocity models beneath the seismic stations TSUM, LSZ, and LBTB (Figures 4i–k). Although we analyzed seismic data recorded at SUR, due to the lack of identifiable phases, we do not generate P- and S-wave velocity models for the station. Similar to most of the results in north and west Africa, our results for southern Africa are representative of stable shield regions. However, in general, we obtain slightly higher crustal thicknesses ranging between  $\sim 42$  km and 46 km (Figures 4i–k). We also predict crustal low velocity zones as discussed later in our models beneath two of the three stations in southern Africa. Beneath TSUM, to our knowledge, no prior velocity model exists. Thus, the velocity model obtained from our study at TSUM is the first of its kind. We obtained a crustal thickness beneath TSUM of  $\sim 42$  km (Figure 4i). The velocities of P- and S-waves in the crust range between 6.3 km/s–7.3 km/s, and 3.2 km/s–4 km/s, respectively (Figure 4i). These results are similar to those obtained for the seismic stations in north and west Africa and are therefore representative of stable shield regions. We do not obtain any anomalous P- and S-wave velocity zones beneath TSUM (Figure 4i). At LSZ, our study indicates that the Moho is located at a depth of  $\sim 43$  km (Figure 4j), which is consistent with that obtained by Midzi and Ottemöller (2001) ( $\sim 40$ –43 km). The crustal P-wave velocity is nearly constant ( $\sim 6.2$  km/s) between  $\sim 8$  km to 32 km depth (Figure 4j). Below  $\sim 32$  km depth, P-wave velocities increase rather sharply from  $\sim 6.2$  km/s to 7.8 km/s at the Moho (Figure 4j). The crustal S-wave velocities range between  $\sim 3.6$  km/s and 3.8 km/s (Figure 4j). We also obtain a lower crustal low-velocity zone of  $\sim 5$ –8 km thickness in our velocity model for LSZ (Figure 4j), consistent with models for seismic stations elsewhere in Africa in the cratonic regions. Such a phenomenon was also noted by Midzi and Ottemöller (2001). Figure 4k shows the P- and S-wave velocity models beneath LBTB obtained in our study. There appears to be a broad crust–mantle transition zone beneath LBTB and the upper bound of the estimate of crustal thickness beneath LBTB is  $\sim 46$  km (Figure 4k). Midzi and Ottemöller (2001) also noted the same and predicted a crust–mantle transition zone between 37–45 km. The crustal P- and S-wave velocities beneath LBTB range between 5.8 km/s–7.5 km/s, and 3.5 km/s–4.2 km/s, respectively, except for a distinct low P-velocity (5.4 km/s) zone of  $\sim 8$  km thickness in the upper crust between 10 km–20 km depth (Figure 4k). Such a low-velocity zone was also obtained by Midzi and Ottemöller (2001) at similar depths, however, the P-wave velocities predicted from our study for this zone are significantly lower than those predicted by Midzi and Ottemöller (2001). Given its appearance beneath other cratonic seismic stations in Africa, the crustal low-velocity zone appears to be a general characteristic of the region.

## **CONCLUSIONS AND RECOMMENDATIONS**

In this paper, we discuss a waveform fitting technique that relies on a parallelized reflectivity method to compute synthetic seismograms and implements a global optimization algorithm using VFSA. We also demonstrate the application of the method to determine one-dimensional, azimuthally dependent, crust and upper mantle P- and S-wave velocity structure beneath broadband seismic stations across the continent of Africa. Our technique avoids dependence of the final results on the initial model, and we are able to compute synthetic seismograms that contain all the possible phases for a prescribed source–receiver path, and obtain direct estimates of the P- and S-wave velocities beneath seismic stations. Statistical tools incorporated in the technique allow us to assess uncertainties associated with our models and estimate tradeoffs between model parameters in different layers. The use of the SPL phase as shown in the study, enhances our constraints for lower crust and upper mantle structure beneath the seismic stations.



Applied to large-magnitude, deep-focus earthquakes recorded teleseismically in Africa, our method successfully produced crust and upper mantle (wherever SPL was observed) P- and S-wave velocity models, that are consistent with earlier models, in the sense that they fall within the associated uncertainties we found with the products of multiple VFSA runs. For some seismic stations, our study provided such velocity models that are the first of their kind. Our models were also consistent with the regional tectonics of Africa. While the technique described here provided layered, one-dimensional models, a dataset that includes a broader azimuthal distribution of earthquakes for each station would allow this source-receiver-based technique to produce better azimuthally-dependent models, and thus a more detailed view of the earth's structure. We plan to apply this method to determine the crust and upper mantle structure beneath China and the Middle East.

### **ACKNOWLEDGEMENTS**

Data were obtained from the Incorporated Research Institutions for Seismology (IRIS).

### **REFERENCES**

- Ammon, C. J. (1991). The isolation of receiver effects from teleseismic P wave fronts, *Bull. Seis. Soc. Am.* 81: 2,504–2,510.
- Ayele, A., G. Stuart, and J. M. Kendall (2004). Insights into rifting from shear wave splitting and receiver functions: An example from Ethiopia, *Geophys. J. Int.* 157: 354–362.
- Berckhemer, H. et al. (1975). *Afar Depression of Ethiopia*, in *Schweizerbart*, Vol. 1, A. Pilger and A. E. Rosler (Eds.). Stuttgart: Schweizerbart'sche Verlagsbuchhandlung, Science Publishers, 89–107.
- Dugda, M. T. and A. A. Nyblade (2006). New constraints on crustal structure in eastern Afar from the analysis of receiver functions and surface wave dispersion in Djibouti, in *The Structure and Evolution of the East African Rift System in the Afar Volcanic Province*, Yirgu, G., C. J. Ebinger, and P. K. H. Maguire (Eds.). London: Geological Society of London, Special Publications, Vol. 259, pp. 241–253.
- Dugda, M. T., A. A. Nyblade, J. Julià, C. A. Langston, C. J. Ammon, and S. Simiyu (2005). Crustal structure in Ethiopia and Kenya from receiver function analysis: Implications for rift development in eastern Africa, *J. Geophys. Res.* 110: B01303, doi:10.1029/2004JB003065.
- Hazler, S. E., A. F. Sheehan, D. E. McNamara, and W. R. Walter (2001). One-dimensional shear velocity structure of northern Africa from Rayleigh wave group velocity dispersion, *Pure Appl. Geophys.* 158: 1,475–1,493.
- Ingber, L. (1989). Very fast simulated reannealing, *Math. Comput. Modeling*, 12: 967–993.
- Kennett, B. L. N. (1983). *Seismic Wave Propagation in Stratified Media*. Cambridge: Cambridge University Press.
- Knox, R., A. Nyblade, and C. Langston (1999). Upper mantle S velocities beneath Afar and western Saudi Arabia from Rayleigh wave dispersion, *Geophys. Res. Lett.* 25: 4,233–4,236.
- Marone, F., M. van der Meijde, S. van der Lee, and D. Giardini (2003). Joint inversion of local, regional and teleseismic data for crustal thickness in the Eurasia-Africa plate boundary region, *Geophys. J. Int.* 154: 499–514.
- Midzi, V. and L. Ottemöller (2001). Receiver function structure beneath three southern Africa seismic broadband stations, *Tectonophysics* 339: 443–454.
- Owens, T. J., S. R. Taylor, and G. Zandt (1987). Crustal structure at regional seismic test network stations determined from inversion of broadband teleseismic P waveforms, *Bull. Seismol. Soc. Am.* 77: 631–662.
- Pasyanos, M. E. and W. R. Walter (2002). Crust and upper-mantle structure of North Africa, Europe and the Middle East from inversion of surface waves, *Geophys. J. Int.*, 149: 463–481.
- Pasyanos, M. E., W. R. Walter, M. P. Flanagan, P. Goldstein, and J. Bhattacharyya (2004). Building and testing an *a priori* geophysical model for western Eurasia and North Africa, *Pageoph.* 161: 235–281.



## 28th Seismic Research Review: Ground-Based Nuclear Explosion Monitoring Technologies

- Pulliam, J. and M. K. Sen (2005). Assessing uncertainties in waveform modeling of the crust and upper mantle, in *Proceedings of the 27th Seismic Research Review: Ground-Based Nuclear Explosion Monitoring Technologies*, LA-UR-o5-6407, Vol. 1, pp. 152–160.
- Sandvol, E., D. Seber, A. Calvert, and M. Barazangi (1998). Grid search modeling of receiver functions: Implications for crustal structure in the Middle East and North Africa, *J. Geophys. Res.* 103: 26,899–26,917.
- Sen, M. K. and P. L. Stoffa (1995). *Global Optimization Methods in Geophysical Inversion*, Netherlands: Elsevier Science Publishing Company.
- Sen, M. K. and P. L. Stoffa (1996). Bayesian inference, Gibbs' sampler and uncertainty estimation in geophysical inversion, *Geophys. Prospecting* 44: 313–350.
- Tiberi, C., C. Ebinger, V. Ballu, G. Stuart, and B. Oluma (2005). Inverse models of gravity data from the Red Sea–Aden–East African rifts triple junction zone, *Geophys. J. Int.* 163: 775–787.